Solar Energy Materials & Solar Cells 252 (2023) 112182

Contents lists available at ScienceDirect

Solar Energy Materials and Solar Cells

journal homepage: www.elsevier.com/locate/solmat

Impact of Li and K co-doping on the optoelectronic properties of CZTS monograin powder

Katri Muska [a,*], Kristi Timmo [a], Maris Pilvet [a], Reelika Kaupmees [a], Taavi Raadik [a], Valdek Mikli [a], Maarja Grossberg-Kuusk [a], Jüri Krustok [a], Raavo Josepson [b], Sven Lange [c], Marit Kauk-Kuusik [a]

[a] Department of Materials and Environmental Technology, Tallinn University of Technology, Ehitajate tee 5, 19086, Tallinn, Estonia
[b] Department of Cybernetics, Tallinn University of Technology, Ehitajate tee 5, 19086, Tallinn, Estonia
[c] University of Tartu, Faculty of Science and Technology, Institute of Physics, Ülikooli 18, 50090, Tartu, Estonia

ARTICLE INFO

Keywords:
Kesterite
CZTS
Doping
Solid solutions
Powder technology
Photoluminescence
Carrier lifetime
Solar cells

ABSTRACT

In this work, the impact of Li and K co-doping on the properties of Cu_2ZnSnS_4 (CZTS) monograin powders used as absorber materials in monograin layer (MGL) solar cells was investigated. CZTS powders were grown in the liquid phase of flux materials with different LiI-KI ratios by synthesis-growth method. According to Atomic Absorption Spectroscopy, the amount of K in the host material did not depend on the molar ratio of LiI to KI in the flux mixtures and remined constant at 0.01 at%. However, the Li concentration depended on the initial amount of LiI in the LiI-KI flux mixture and increased from 0.01 at% to 1.22 at% in the synthesized CZTS. X-ray diffraction, Raman analysis and photoluminescence (PL) analysis confirmed that Li content $x = 0.2$ and $x = 0.4$ in the input composition of $(Cu_{1-x}Li_x)_{1.84}Zn_{1.09}Sn_{0.99}S_4$ resulted in formation of solid solution. The external quantum efficiency measurements showed that the effective bandgap energy of CZTS increased from 1.52 eV to 1.57 eV by increasing the Li content in CZTS from $x = 0$–0.02 to $x = 0.4$, respectively. The mean values of V_{OC} of the corresponding monograin layer solar cells increased from 700 to 742 mV. The highest V_{OC} of 784 mV was obtained with device based on solid solution containing 1.22 at% of Li ($x = 0.4$). The best performing solar cell with power conversion efficiency of 9.4% was obtained with Li and K co-doped CZTS powder ($x = 0.002$) showing output parameters: $V_{OC} = 718$ mV, $J_{SC} = 20.9$ mA/cm^2 and $FF = 62.5\%$.

1. Introduction

The development of new materials for solar energy harvesting is currently one of the major research topics in the field of renewable energy, although it has been an active area of research for more than half a century [1]. Kesterite $Cu_2ZnSn(S,Se)_4$ (CZTSSe) materials have attracted considerable interest as a promising candidate for future large-scale deployment of the photovoltaics. They are produced from earth-abundant, non-toxic constituents, having thermodynamically stable structure, and large potential for high power conversion efficiency (PCE) defined by its suitable optoelectronic properties. The theoretical Shockley-Queisser (SQ) limit of kesterites is ~30%, however the open circuit voltage (V_{OC}) deficit continues to be a key problem with the record cell reaching only 62.6% of its SQ limit [2].

Perspective strategy to improve the PCE of the kesterite solar cells is doping of absorber material with alkali and other related metals [3]. However, the optimal doping concentration of different alkali elements in kesterite materials is uncertain. An improvement of the electronic properties by adding extrinsic elements to the kesterite matrix in various quantities has been inspired by the related CIGS technologies, where the band structure engineering through substitutional doping with alkali metals boost the solar cell efficiencies beyond 22% [4].

Based on potassium and lithium properties, both could be located on the Cu positions within the kesterite lattice. However, previous studies about the localization of K in chalcogenide absorber layers by atom probe tomography revealed that K is segregating at the grain boundaries [5]. Due to the large K^+ ionic radius (1.51 Å) and thus a high substitution energy of 1.53 eV, alloying of K within the kesterite lattice is unlikely [6]. K doping have been found to increase the carrier concentration and to reduce the series resistance of solar cell devices

* Corresponding author.
E-mail address: katri.muska@taltech.ee (K. Muska).

https://doi.org/10.1016/j.solmat.2023.112182
Received 29 July 2022; Received in revised form 22 December 2022; Accepted 2 January 2023

based on K doped samples as compared to untreated samples [3]. Recent studies on Li incorporation have demonstrated the most positive impact on optoelectronic properties of CZTSSe among all the alkali elements [3]. As the crystallographic ionic radius of Li^+ is very close to the isovalent Cu (0.6 Å for Li^+ vs 0.59 Å for Cu^+) [7], Li has more possibility to be incorporated into the kesterite lattice and to modify the defect properties compared to other alkali elements. Li has been mostly directly incorporated into CZTSSe precursors and involved in the grain growth [8]. The performance enhancement resulted from Li incorporation has been generally attributed to the improved crystallinity, reduced grain boundary recombination, increased *p*-type doping, and modified interface with more Cu-depleted surface [9]. Incorporation of Li into CZTSSe thin films is also reported to decrease both the conduction band minimum and valence band maximum, which results in an increasing conduction band offset at the CdS/$Cu_{2-x}Li_xZnSn(S,Se)_4$ interface [10]. Li incorporation into the lattice of CZTS increases the band gap energy value [1,10,11] and slightly increased the record efficiency of CZTSSe to 12.7% after years of being stagnated at 12.6% [12].

In this study, a molten salt synthesis-growth method for producing pure Cu_2ZnSnS_4 (CZTS) single-crystalline semiconductor powder (so-called monograin powders) was used. The synthesis temperature is limited by two melting points - $T_{synth} > T_{melt(salt)}$ and $T_{synth} < T_{melt\ (semiconductor)}$. This powder is formed in the presence of the liquid phase of inorganic halide salts (KI, LiI and the mixtures of KI-LiI) at relatively high temperatures ($T_{synth} = 740$ °C) because e.g. $T_{melt(KI)} = 681$ °C [13]. Therefore, the formed semiconductor crystals are unintentionally doped with the constituent elements from salt (e.g. K, Li and I). The level of doping depends on the time and temperature of heating and is limited by the solubility of the dopant in the matrix crystal in the conditions sufficient for saturation. Several studies have found that incorporation of Li into kesterite is sensitive to Na, so that Li alloying is more easily achieved without Na [14,15]. However, so far there are no consistent experimental results concerning the impact of the constituent elements from salt on the kesterite single-crystalline powder properties and monograin solar cell device performance. Although, the influence of several extrinsic dopants and different alloying strategies on the performance of the CZTS monograin layer solar cells have been already investigated (Table S1). All high efficiency CZTS monograin layer solar cells are based on the powders, which are synthesized in KI [16]. Therefore, these powders always contain a certain amount of potassium. In this study, impact of the co-doping of K and Li on the optoelectronic properties of CZTS monograin powder and device performance was investigated. The extrinsic doping levels in CZTS powder crystals were modified by using different salt mixtures in the synthesis process.

2. Experimental

2.1. Synthesis of monograin powders and preparation of solar cells

The quaternary compound monograin powders with initial composition $Cu_{1.84}Zn_{1.09}Sn_{0.99}S_4$ were synthesized in the liquid phase of a flux material. For the flux material, pure KI and the mixture of LiI and KI with 0.08, 0.74, 7.34 and 14.47 M % of LiI from KI was used. The corresponding Li contents in $(Cu_{1-x}Li_x)_{1.84}Zn_{1.09}Sn_{0.99}S_4$ material are x = 0.002, x = 0.02, x = 0.2 and x = 0.4. Hereinafter, the x values are used as the sample names. All powders were synthesized using high purity (99.999%) precursors. Binary precursors CuS and SnS were self-synthesized from commercially available elemental Cu shots, Sn shots and S powder, respectively. ZnS was purchased as a binary compound. The precursors and the flux material were mixed in mass ratio of 1:1 and inserted into a quartz ampoule, which was then degassed and closed under dynamic vacuum. Due to the hygroscopic nature of LiI, the mixing of precursors was done in a glove box in dry argon environment.

Although, the formation of CZTS compound already starts at around 450 °C, the main CZTS monograins growth and homogenization occur after the melting of the flux material. The melting temperature of KI is 681 °C and the melting temperature of LiI is 469 °C [17], but according to phase diagrams of the binary system LiI-KI [18] even lower melting temperatures can be achieved by forming a eutectic mixture. Therefore, lower synthesis temperatures could be potentially used for monograin powder growth when LiI is used together with KI flux. While in this study one sample was prepared in pure KI and to keep similar process conditions, all the monograin powders were synthesized in muffle oven at 740 °C for 136 h. More information about monograin powder growth mechanisms can be found elsewhere [19].

After the synthesis-growth, ampoules were naturally cooled to room temperature approximately within an hour, opened, and the flux material was removed by washing the powders with distilled water. The sedimented solid powder crystals were then dried in hot-air oven at 50 °C. After drying, a sieving analysis method was used to sieve the powders into narrow granulometric fractions, as well as to study the particle size distribution of the monograin powders. Sieving was conducted by sieving system Retsch AS 200 for 30 min. From the sieving analysis median grain size (D_{50}) was determined. The useful fraction sizes for further implementation in monograin layer solar cells in laboratory conditions are between 36 and 125 μm. More detailed description about sieve analysis of monograin powders is brought in Ref. [20].

Before implementing the monograins as absorber layer in monograin layer (MGL) solar cells with the structure of Au/CZTS/CdS/*i*-ZnO/ZnO:Al/Ag/glass, the powder crystals needed subsequent post-treatments. At first, the powder crystal surfaces were cleaned and modified by etching for 5 min with 1% v/v Br_2–MeOH solution followed by etching with 10% m/m KCN solution for 5 min. Etched monograins were subsequently post-annealed in a dual-zone tube furnace at 840 °C in sulfur atmosphere ($P_S = 2050$ Torr) for 60 min. The post-treated crystals were covered with cadmium sulfide (CdS) buffer layer by chemical bath deposition to form heterojunction. CdS was deposited from alkali solution containing 0.01 M cadmium iodide (CdI_2), 1 M thiourea ($SC(NH_2)_2$), and 2 M ammonia aqueous solution (NH_4OH). After buffer layer deposition, a soft-annealing at 200 °C for 10 min was applied. CdS covered CZTS powder crystals were partially embedded into a polymer layer drawn on a transparent substrate to form the so-called monograin membrane. After complete polymerization, the membrane was covered with *i*-ZnO/ZnO:Al window layer by radio-frequency magnetron sputtering process. After applying Ag-paste as front collector, the structure was glued on a glass using transparent polymer to seal the front side. For back contact gold squares were thermally evaporated using a metal stencil with single cell area of 4.5 mm^2. Before evaporating the back contacts, the MGL was etched with H_2SO_4 and polished with sand paper to remove polymer and CdS layers from the back of the monograins. More detailed description of the post-treatment and device preparation can be found in Ref. [21].

2.2. Characterization methods

The morphology of as-grown powder crystals was studied by high-resolution scanning electron microscopy (HR-SEM Zeiss Merlin). The composition of the main constituent elements in the post-annealed powder crystals was analyzed by energy dispersive X-ray spectroscopy (EDX) on HR-SEM Zeiss Merlin equipped with Bruker EDX-XFlash6/30 detector with an accelerating voltage of 20 kV.

The concentration of extrinsic dopants- Li and K in the post-annealed CZTS monograins were analyzed by atomic absorption spectroscopy (AAS). Spectra AA 220F and 220Z atomic absorption spectrometers (Varian, Mulgrave, Australia) equipped with a side-heated GTA-110Z graphite atomizer, a Zeeman effect background correction, and an integrated autosampler were used.

Phase composition of the post-annealed CZTS powder crystals were measured by room-temperature (RT) micro-Raman spectroscopy using Horiba's LabRam HR 800 spectrometer equipped with a multichannel CCD detector in the backscattering configuration using a 532 nm laser line.

Crystal structure of post-annealed CZTS powders was determined by

X-ray diffraction (XRD) using a Rigaku Ultima IV diffractometer with monochromatic Cu Kα radiation $\lambda = 1.54056$ Å at 40 kV and 40 mA, using a D/teX Ultra silicon strip detector.

The photoluminescence spectroscopy (PL) was used to study the changes in the defect structure of differently doped CZTS powders. The post-annealed CZTS powders were mounted in a closed-cycle He cryostat enabling variation of temperature between 10 and 300 K. The 442 nm He–Cd laser line was used as an excitation source and its intensity was attenuated with a range of neutral density filters. A cooled InGaAs detector and the PMT R632 from Hamamatsu were used to detect the PL signal.

The current-voltage (*I–V*) measurements at room temperature were performed under AM 1.5 (100 mW/cm^2) illumination condition using a Newport Oriel Class A 91195A solar simulator system. *I–V* characteristics were recorded by a Keithley 2400 source meter. The *I–V* (*T*) curves were measured with a Keithley 2401 Source Meter under 100 mW/cm^2 illumination using calibrated intensity from a halogen lamp. The temperature-dependent measurements were performed in the closed-cycle He cryostat. As the working area of the MGL solar cells is around 75% of the total area [16], the MGL solar cell efficiency values were re-calculated for the active area (η_{active}).

The external quantum efficiency (EQE) spectra were performed on a commercial EQE measurement system (Canada, Sciencetech Inc., PTS-2-IQE). The light intensity at each wavelength was calibrated by a calibrated pyroelectric detector. The measurements were done at no bias light condition, and at 0V bias voltage.

The time-resolved photoluminescence (TRPL) measurements for the post-annealed CZTS powders were done through an optical microscope (50x magnification) capable of exciting the sample with focused laser light and gathering the PL at the same time. For excitation 635 nm pulsed solid-state laser (ALDS model PiL063X, repetition rate 4 MHz, pulse width 40 ps and average power 1 W). The PL signal was collected from microscopes exit focal plane by an optical fiber and directed to Andor SR303i spectrograph with single point avalanche photodiode as detector positioned roughly in the center of the PL emission band at 900 nm. The photon generated electrical impulses from the avalanche diode were time integrated with PicoHarp 300 multichannel counter with timeslot resolution of 8 ps.

3. Results and discussion

The bulk composition of the post-annealed CZTS monograin powders grown in different flux mixtures was studied by EDX and AAS, and the results are summarized in Table 1. The content of alkali elements in the post-annealed CZTS was analyzed by a very sensitive method AAS, which allows to measure the elements at parts per million (ppm) level. According to EDX and AAS analysis, the Cu/Sn ratio in the synthesized CZTS decreased from 1.90 to 1.87 by increasing the Li content in the precursor mixture. The ratio (Cu + Li)/(Zn + Sn) increased from 0.91 to 0.96 in CZTS powders by increasing the Li content and this is strong indication about the formation of a solid solution of $(Cu_{1-x}Li_x)_2ZnSnS_4$.

According to AAS analysis, all powders were doped with K at the similar level of 0.01 at% in CZTS. Therefore, it could be the saturated concentration of K in CZTS at 740 °C. AAS results confirmed that there is a clear correlation between LiI content in the starting flux material and Li content in the synthesized CZTS material. Results showed that Li concentration in CZTS increased from 0.01 at% to 1.22 at% by increasing the content of LiI in LiI-KI mixture. According to Ref. [3], the term "doping" is used if the concentration of extrinsic element does not exceed 1 mol% without changing the host material structure. Based on AAS results, it can be stated that solid solutions with the chemical formulas $(Cu_{1-x}Li_x)_{1.96}Zn_{1.09}Sn_{1.02}S_4$ (x = 0.0331) and $(Cu_{1-x}Li_x)_{2.0}Zn_{1.07}Sn_{1.02}S_4$ (x = 0.0494) have been formed in the case of CZTS powders with an input of x = 0.2 and x = 0.4, respectively.

The formation of solid solutions was confirmed also by XRD and Raman analysis. The results are presented in Fig. 1 and Fig. 2, respectively. All XRD patterns of the CZTS monograins exhibited diffraction peaks belonging to the kesterite Cu_2ZnSnS_4 phase with the space group *I-4* (ICDD:01-084-8521). Main characteristic peaks are attributed to (112), (220), and (312/116) planes [22]. In addition to the main reflections, the Rietveld analysis also indicated to the presence of small amount of ZnS (ICDD: 01-083-2124) in the monograins. The diffraction peak (112) shifts to lower diffraction angles with increasing Li concentration in CZTS from 28.488° (x = 0) to 28.417° (x = 0.2). Small shift was also observed in the other diffraction peaks with increasing the Li content in CZTS. According to the theoretical calculation, the covalent radius of Li (1.33 Å) is larger than that of Cu (1.27 Å) and Zn (1.22 Å). Therefore, replacing Cu or Zn places in the kesterite lattice by Li ions results in a longer lithium–sulfur bonding distance, thus shifting the XRD Bragg refection to lower 2Θ values [23].

Calculated lattice parameters *a, b* and *c* increased with increasing the Li content from x = 0 to x = 0.4 in input composition of CZTS from $a = b = 5.430$ Å to $a = b = 5.439$ Å and $c = 10.831$ Å to $c = 10.839$ Å, respectively. It has been found, that Cu-vacancies are energetically favorable defects in the Cu-poor and Zn-rich kesterite materials. The Cu-vacancies are preferentially located at *2a* sites and therefore, the shift in the diffraction angle together with the increase of parameter *a*,

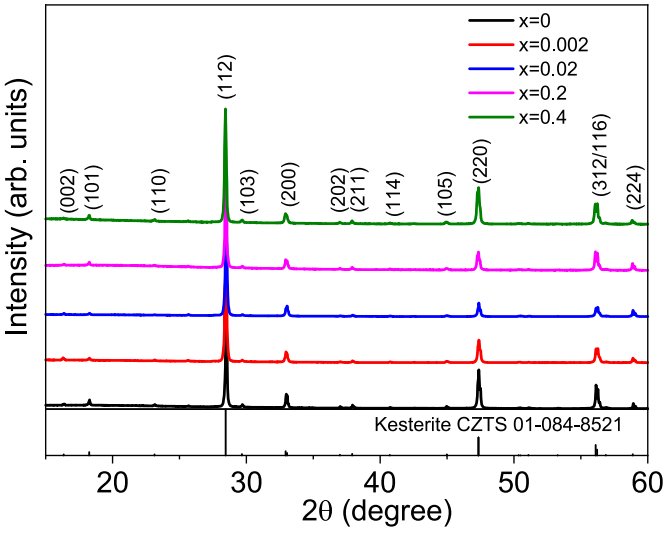

Fig. 1. XRD patterns of post-annealed CZTS monograin powders with different Li concentration in the input composition.

Table 1
Elemental composition of the CZTS powders after post-annealing analyzed by AAS (K, Li) and by EDX (Cu, Zn, Sn, S).

Sample name	x in CZTS	Elemental composition, at %						Chemical formula
		[Li]	[K]	[Cu]	[Zn]	[Sn]	[S]	
x = 0	–	–	0.01	23.85	13.57	12.57	50.00	$Cu_{1.91}Zn_{1.09}Sn_{1.01}S_4$
x = 0.002	0.0004	0.01	0.01	24.02	13.30	12.65	50.01	$(Cu_{1-x}Li_x)_{1.92}Zn_{1.06}Sn_{1.01}S_4$
x = 0.02	0.0037	0.09	0.01	23.89	13.43	12.61	49.97	$(Cu_{1-x}Li_x)_{1.91}Zn_{1.08}Sn_{1.01}S_4$
x = 0.2	0.0331	0.81	0.01	23.52	13.50	12.59	49.58	$(Cu_{1-x}Li_x)_{1.96}Zn_{1.09}Sn_{1.02}S_4$
x = 0.4	0.0494	1.22	0.01	23.54	13.22	12.61	49.40	$(Cu_{1-x}Li_x)_{2.0}Zn_{1.07}Sn_{1.02}S_4$

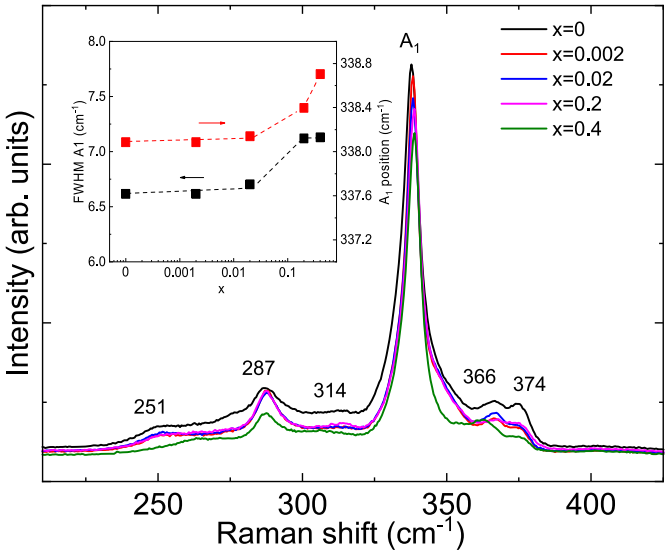

Fig. 2. RT Raman spectra of post-annealed CZTS monograin powders with different Li concentration in the input composition and the inset graph shows A_1 Raman peak position and FWHM for A_1 mode depending on x value.

correlates to the incorporation of Li into the kesterite [24].

In order to support the results obtained from XRD about the possible incorporation of Li into the CZTS powders by using LiI in the LiI- KI flux mixtures, the Raman analysis was performed. Raman spectra of the post-annealed CZTS monograin powders with different x values are presented in Fig. 2. All Raman peaks correspond to the kesterite CZTS phase with dominant A_1 Raman peak at approximately 338 cm^{-1} [25].

The inset graph in Fig. 2 shows A_1 Raman peak position and full width half maximum (FWHM) for A_1 mode depending on x value. The FWHM of the A_1 mode is increasing from ~6.6 cm^{-1} to 7.1 cm^{-1} by increasing the Li content in precursor mixture to x = 0.1 and x = 0.2. The small FWHM indicates to good crystallinity of the monograins [26]. The shift of A_1 mode from 338.1 cm^{-1} to higher wavenumbers for CZTS powders with x = 0.1 and x = 0.2 also indicates to the formation of solid solutions.

Fig. 3 shows the SEM images of as-grown CZTS monograin powders with fraction size 75–80 μm synthesized in different flux mixtures. It was seen that all the powder crystals inhibited tetrahedral crystal shape and it did not really depend on the content of Li in the CZTS. The shape of the individual grains is influenced by the solubility of formed quaternary compound in the flux material. CZTS solubility is probably higher in LiI than in KI [27], but the amount of LiI used for the synthesis of the monograins in the current study was not sufficient to have a visible effect on the morphology of the grains.

The particle size distribution was analyzed by sieving analysis method and revealed that the median grain size was very similar for all the CZTS powders grown in different LiI-KI flux mixtures. Therefore, it could be concluded that increasing the content of Li in the range of x = 0 to x = 0.4 in CZTS does not influence the monograin powder growth particularly.

The influence of K and Li co-doping effect on the defect structure and related recombination processes in CZTS monograins were studied by low-temperature photoluminescence spectroscopy. PL spectra of the post-annealed CZTS with different Li content are shown in Fig. 4a. All PL spectra consist of at least two asymmetric PL bands regardless of Li content. The spectra were fitted using a split Gaussian function (Fig. 5).

The first peak, at around 1.27 eV (#D2) is present in all materials, thus it is not linked to the Li. The other peak around 1.33 eV (#D1) is present for both, the CZTS material without Li (Fig. 5a) and for CZTS materials with different Li content (Fig. 5b and c). At higher Li concentrations (x = 0.2 and x = 0.4), the peaks #D2 and #D1 shift to higher energies (Fig. 4b) and an additional asymmetrical PL peak at 1.33 eV (#D1*) appears (Fig. 5c).

The #D1* peak seems to be associated to the Li and can be connected to the formation of solid solution. To determine the type of recombination, the laser power dependencies of the PL emission were measured (figure not shown). It is known, that the integrated intensity $\Phi(P)$ of PL band depends on the excitation laser power P as $\Phi \sim P^m$. The power coefficient m can be found as the gradient of the $\Phi(P)$ plot on a log-log scale. All samples showed values m = 0.8–0.9 and this is a direct indication, that defect levels are involved in the recombination process [28]. All samples showed also a peak position shift with laser power in the range of 10–15 meV per decade of laser power, i.e. electrostatic

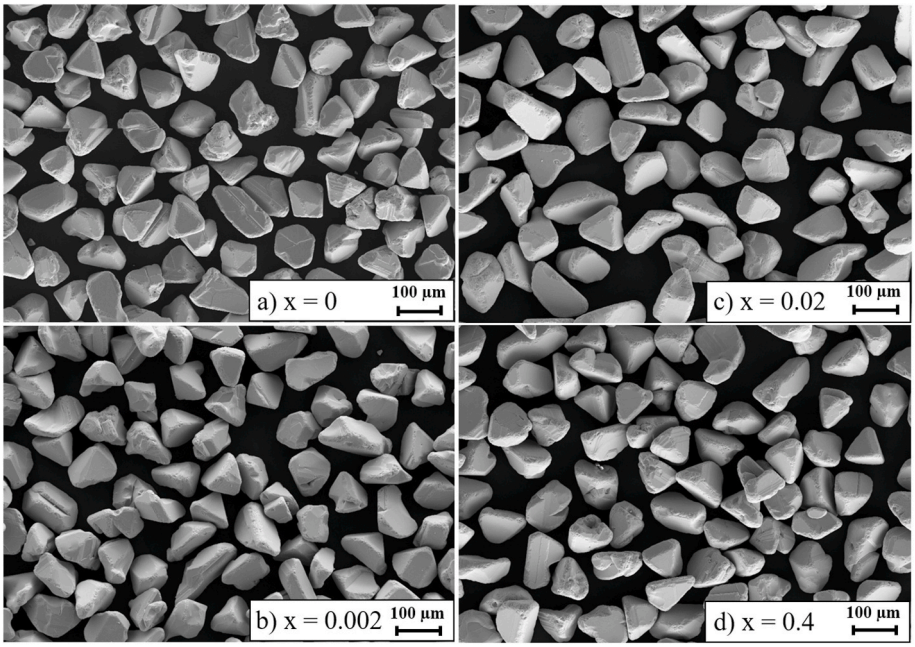

Fig. 3. SEM images of as-grown CZTS materials grown in a) pure KI and b-d) in different Li-KI flux mixtures with x as the Li concentration in the input composition of CZTS.

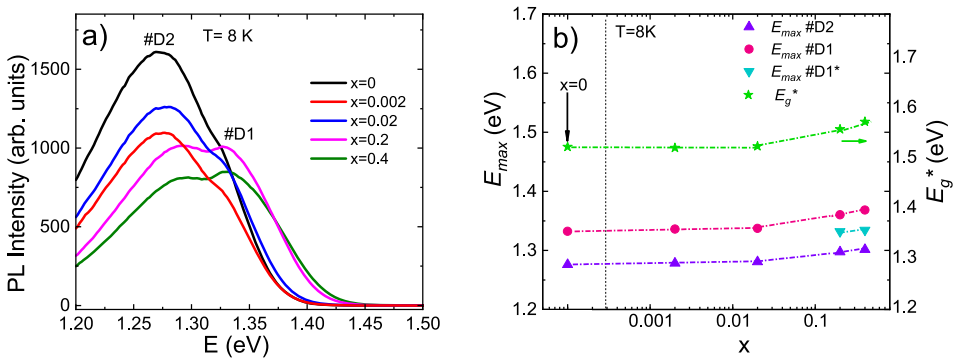

Fig. 4. (a) PL spectra of post-annealed CZTS monograins with different Li concentration in the input composition of CZTS and (b) the corresponding PL peak positions together with the bandgap values determined by EQE analysis.

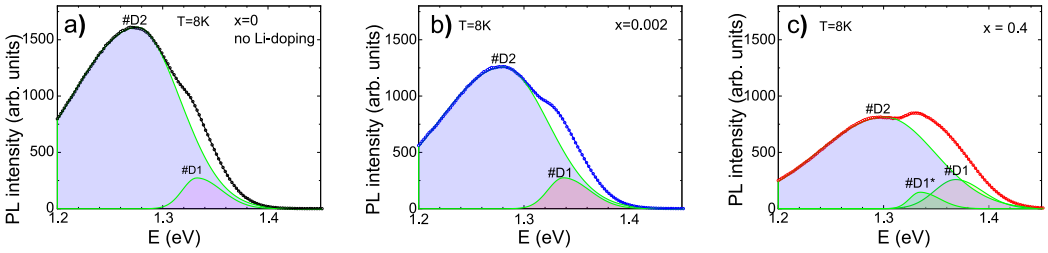

Fig. 5. Split Gaussian function fittings of the PL spectra of the CZTS monograin powders a) without Li (x = 0), and with different Li concentration in the input composition b) x = 0.002 and c) x = 0.4.

potential fluctuations affect radiative recombination [29].

Next, the temperature quenching analysis of PL emission band #D2 was performed. Arrhenius plot of the resulting integral intensity was fitted using a model of single recombination channel and assuming the temperature dependence of the hole capture cross section proposed in Ref. [30]:

$$\Phi(T) = \Phi_0 \,/\, \left[1 + \alpha_1 T^{3/2} + \alpha_2 T^{3/2}\, exp(-E_A \,/\, kT)\right] \quad (1)$$

where φ_0 is the integral intensity of the PL band at 0 K, α_1 and α_2 are process rate parameters and E_A is the activation energy. Thermal quenching activation energy E_A of PL emission as a function of Li content x in the input composition of $(Cu_{1-x}Li_x)_{1.84}Zn_{1.09}Sn_{0.99}S_4$ in presented in Fig. 6. The activation energy E_A is increasing with increasing the value x

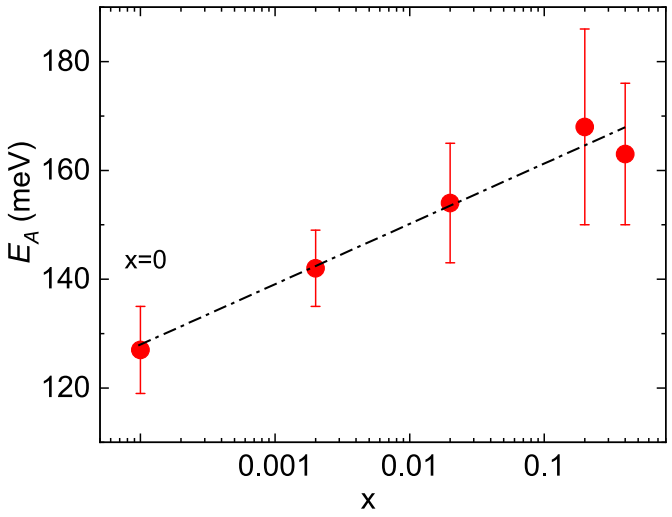

Fig. 6. Thermal quenching activation energy E_A of PL emission as a function of Li content x in the input composition of CZTS.

and this can be an indication that the depth of acceptor defects is increasing with Li concentration. This is possible in case of deep donor-deep acceptor (DD-DA) pair model [31,32], where the distance between very close donor and acceptor defects determines the position of energy levels. It is known, that the PL peak energy for every single DA pair recombination is expressed as:

$$E_i(r) = E_g - (E_d + E_a) + \frac{e^2}{\varepsilon r_i} \quad (2)$$

where E_g, E_d and E_a are the band gap energy, and the donor and acceptor ionization energies, respectively, r_i is the distance between the donor and acceptor defects, and ϵ is the static dielectric constant [33]. Close pairs have shallower acceptor levels (and donor levels) than pairs with larger distances due to a Coulomb term in Eq. (2). As the lattice parameters of CZTS are increasing with Li concentration, the distances between possible acceptor and donor defects are also increasing leading to the increase of acceptor level ionization energy.

The post-annealed CZTS monograins with different Li concentration were used as absorber layers in MGL solar cells. The *J–V* characteristics of the devices measured under illumination and obtained output parameters are presented as box plots in Fig. 7. The average value is calculated from 15 solar cells. The mean values of V_{OC} increase from 700 to 742 mV by increasing the Li content from x = 0 to x = 0.4 in the input composition of $(Cu_{1-x}Li_x)_{1.84}Zn_{1.09}Sn_{0.99}S_4$. The highest V_{OC} of 784 mV was obtained with device based on solid solution containing Li 1.22 at% (measured by AAS). This is in good correlation with literature [24], that Li can be incorporated within the kesterite phase in much higher quantities than K forming solid solutions, which offers a way for tuning the CZTS bandgap.

The mean values of short circuit current density (J_{SC}) fluctuate in the range of 17.8 mA/cm^2 (x = 0) to 18.7 mA/cm^2 (x = 0.002). The highest J_{SC} of 21.8 mA/cm^2 was obtained with device based on CZTS co-doped with K and Li (both 0.01 at% measured by AAS). The values of FF decreased by increasing the Li content in the input composition of $(Cu_{1-x}Li_x)_{1.84}Zn_{1.09}Sn_{0.99}S_4$.

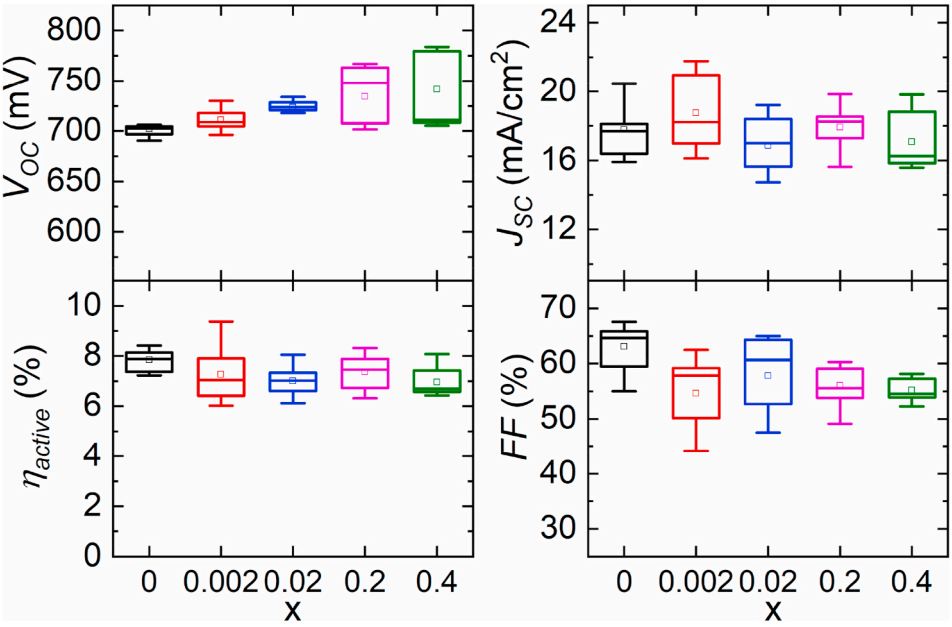

Fig. 7. Box-plot diagram of CZTS solar cell parameters a) open circuit voltage (V_{OC}), b) current density (J_{SC}), c) efficiency (η_{active}) and d) fill factor (FF) with different Li concentration in the input composition of CZTS.

CZTS monograin layer solar cell based on powder grown in KI (no Li) showed the highest power conversion efficiency (PCE) of 8.4% with following parameters: the open circuit voltage (V_{OC}) value of 702 mV, short circuit current density (J_{SC}) of 20 mA/cm^2 and fill factor (FF) of 59%. The best performing solar cell with PCE of 9.4% was obtained with Li and K co-doped CZTS powder (x = 0.002 in the input $(Cu_{1-x}Li_x)_{1.84}Zn_{1.09}Sn_{0.99}S_4$) showing output parameters: V_{OC} = 718 mV, J_{SC} = 20.9 mA/cm^2 and FF = 62.5%.

It is highly possible, that with higher Li content in the CZTS, the conduction band offset changes, thus leading to a mismatch between CdS buffer layer and absorber layer. The other option is that the absorber material needs different post-treatment conditions before the buffer layer deposition and therefore further optimization is needed in the future or an alternative buffer layer would be more suitable.

External quantum efficiency (EQE) measurements were performed to determine the bandgap of the studied absorber materials. Fig. 8 shows the EQE spectra for the solar cells with different Li content CZTS. Near the absorption edge the bandgap energy determination can be done using the following equation [34]:

$$EQE \approx K\alpha L_{eff} \approx A\left(E - E_g^*\right)^{\frac{1}{2}} \Big/ E, \tag{3}$$

where E_g* is an effective bandgap energy and constant A includes all parameters that do not depend on E. Therefore (E*EQE)^2 vs. E curves (inset graph in Fig. 8) should have a linear segment from which one can find a value for E_g*. According to EQE measurements, the effective bandgap E_g* was determined to be ~1.52 eV for CZTS powders with x = 0 to 0.02 in the input composition of $(Cu_{1-x}Li_x)_{1.84}Zn_{1.09}Sn_{0.99}S_4$. The bandgap of absorber material increased to 1.560 eV and to 1.575 eV by increasing the Li content x ≥ 0.2 in the input composition. These results confirm the XRD, Raman and PL results that CZTS powders x = 0 to 0.02 in the input composition of $(Cu_{1-x}Li_x)_{1.84}Zn_{1.09}Sn_{0.99}S_4$ are containing K and Li at the doping level, but further increase of Li will lead to formation of solid solution.

The formed solid solution enlarges the band gap of absorber material, both VBM and CBM shift to lower energy, but the downshift of CBM is less pronounced, which leads to this band gap enlargement [10]. So, it is expected to improve the V_{OC} of CZTS solar cells. The highest V_{OC}

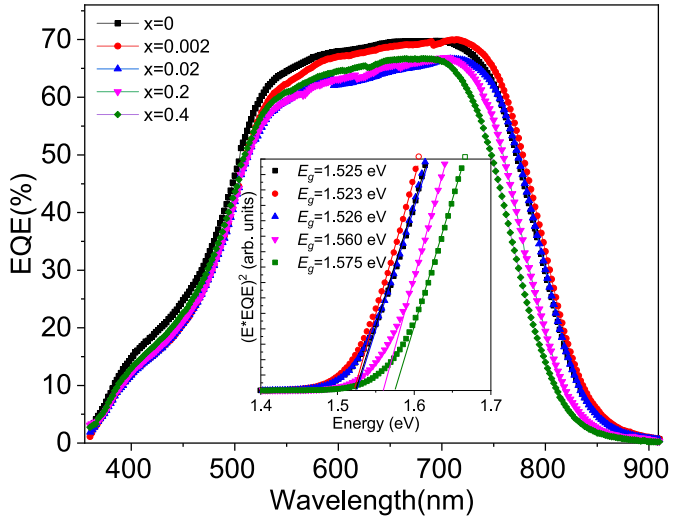

Fig. 8. EQE curves of MGL solar cells based on CZTS monograins with different Li concentration in the input composition of CZTS. Inset graph shows bandgap extraction by plotting (E*QE)^2 vs. photon energy. Solid lines are fitting results using Eq. (3).

Table 2
The highest V_{OC} of CZTS solar cells, absorbers effective bandgap values (E_g*), V_{OC} deficit, activation energies (φ_B), charge separation (τ_1) and minority carrier lifetime (τ_2) from TRPL measurements.

Sample	$V_{OC(max)}$, mV	E_g*, eV	E_g/q-V_{OC}, mV	φ_B, eV	τ_1, ns	τ_2, ns
x = 0	721	1.525	804	1.289	0.15 ± 0.008	0.53 ± 0.1
x = 0.002	729	1.523	794	1.268	0.14 ± 0.001	0.48 ± 0.01
x = 0.02	734	1.526	792	1.264	0.14 ± 0.002	0.48 ± 0.01
x = 0.2	761	1.560	799	1.306	0.14 ± 0.002	0.51 ± 0.01
x = 0.4	784	1.575	791	1.259	0.18 ± 0.006	0.64 ± 0.07

values and calculated V_{OC} deficits are presented in Table 2. The V_{OC} deficits are calculated in this paper with respect to the effective band gap energy values from EQE. Then, $V_{OC\ def} = E_g^*/q\text{-}V_{OC}$. It is seen that although the V_{OC} values increase with Li addition, the V_{OC} deficit remained still large.

The temperature dependence of V_{OC} is often used to determine the dominating recombination processes in solar cells. It is known, that the behavior of the V_{OC} of the cells as a function of the temperature V_{OC} (T) can be described by Eq. (4) [33]:

$$V_{OC} = \frac{\varphi_B}{q} - \frac{Ak_BT}{q}\ln\left(\frac{J_{00}}{J_L}\right), \quad (4)$$

where φ_B is the activation energy, q is the elementary charge, A is the ideality factor, k_B is the Boltzmann constant, T is the temperature, J_{00} is the reverse saturation current pre-factor and J_L is the light generated photocurrent density. At temperatures $T > 200$ K, the V_{OC} versus T shows linear behavior. The extrapolation of this linear part to $T = 0$ K indicates the activation energy φ_B. The calculated φ_B of all devices according to Eq. (4) are given in Table 2 and all these values are smaller than the bandgaps gained from EQE. This means that the interface recombination dominates in all our solar cells and it does not depend much on added Li concentration.

TRPL analysis offers an efficient contactless method to explore recombination and minority carrier lifetimes in absorber layers. Previous studies have found that the PL decay from thin film absorbers may be described using a double-exponential function [35].

$$I(t) = \alpha_1\ exp\left(-t/_{\tau_1}\right) + \alpha_2\ exp\left(-t/_{\tau_2}\right) \quad (5)$$

where $I(t)$ is the PL intensity as a function of time after a fast laser pulse, α_1 and α_2 are intensity coefficients, and τ_1 and τ_2 are decay times, which correspond to the initial and final section of the decay curves, respectively. The first decay time τ_1 is usually considered as an effect of charge separation, while the carrier lifetime is related to τ_2 [36]. The obtained τ_1 and τ_2 values are given in Table 2 and the PL decay curves of K and Li co-doped CZTS monograins are shown in Fig. 9. It is evident that the minority carrier lifetime (τ_2) stays relatively stable.

4. Conclusions

In this study was shown that by controlling the LiI content in LiI-KI flux mixture during the synthesis-growth of Cu_2ZnSnS_4 monograins, it is possible to control the incorporation of Li into Cu_2ZnSnS_4 monograins leading to K and Li co-doping. According to AAS analysis, the concentration of K was 0.01 at% in all synthesized materials independent of used flux mixtures. Li content of x = 0.2 and x = 0.4 in the input composition of $(Cu_{1-x}Li_x)_{1.84}Zn_{1.09}Sn_{0.99}S_4$ resulted in Li concentration about 1 at% in synthesized CZTS material and led to the formation of solid solutions with chemical formulas $(Cu_{1-x}Li_x)_{1.96}Zn_{1.09}Sn_{1.02}S_4$ (x = 0.0331) and $(Cu_{1-x}Li_x)_{2.0}Zn_{1.07}Sn_{1.02}S_4$ (x = 0.0494), respectively.

Structural analysis by XRD and Raman also confirmed the formation of solid solutions if added Li content x in precursor mixture was 0.2–0.4. XRD diffraction peaks shifted to lower diffraction angles and the lattice parameters increased. Also, Raman analysis showed a slight shift of A_1 mode and broadening of A_1 peak FWHM with increasing Li content x in CZTS. According to EQE measurements, the effective bandgap E_g^* was determined to be ~1.52 eV for CZTS powders with x = 0 to 0.02 in the input composition of CZTS. The bandgap of absorber material increased to 1.575 eV by increasing the Li content x ≥ 0.2 in the input composition. PL spectra consisted of two peaks at around 1.27 eV (#D2) and 1.33 eV (#D1) for K-doped CZTS and for K and Li co-doped CZTS. At higher Li concentrations (x > 0.2), the peaks #D2 and #D1 shifted to higher energies and an additional asymmetrical PL peak at 1.33 eV (#D1*) appeared. It was shown that the PL emission of all samples was most probably dominated by the same deep donor-deep acceptor complex.

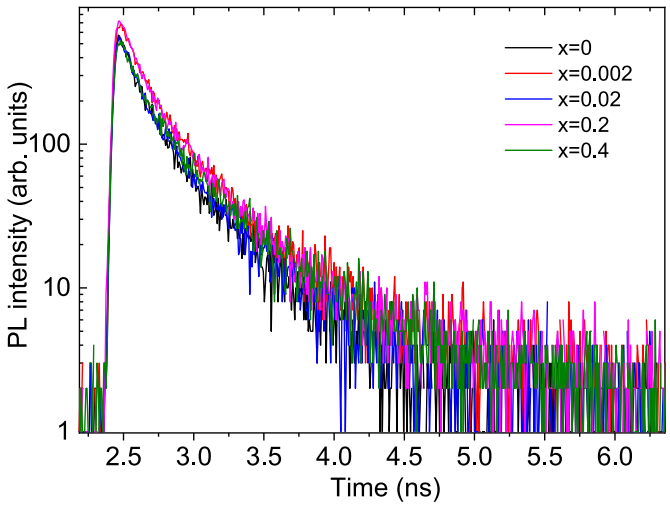

Fig. 9. Average TRPL decay curves of post-annealed CZTS monograins with different Li concentration in the input composition of $(Cu_{1-x}Li_x)_{1.84}Zn_{1.09}Sn_{0.99}S_4$.

The photovoltaic characteristics showed that the addition of Li into CZTS absorber mostly affected the V_{OC} value, which increased from 721 mV to 784 mV. The highest efficiency monograin layer solar cell of 9.4% was achieved with absorber material, which was co-doped with K and Li at the level 0.01 at% in the synthesized CZTS.

CRediT authorship contribution statement

Katri Muska: Writing – original draft, Validation, Project administration, Investigation, Formal analysis, Data curation, Conceptualization. **Kristi Timmo:** Methodology, Investigation. **Maris Pilvet:** Methodology, Investigation. **Reelika Kaupmees:** Methodology. **Taavi Raadik:** Methodology. **Valdek Mikli:** Methodology. **Maarja Grossberg-Kuusk:** Writing – review & editing, Funding acquisition. **Jüri Krustok:** Writing – review & editing, Methodology. **Raavo Josepson:** Methodology. **Sven Lange:** Methodology. **Marit Kauk-Kuusik:** Writing – review & editing, Methodology, Funding acquisition, Conceptualization.

Declaration of competing interest

The authors declare that they have no known competing financial interests or personal relationships that could have appeared to influence the work reported in this paper.

Data availability

Data will be made available on request.

Acknowledgements

This work was supported by European Union through the European Regional Development Fund, Project TK141, and by the Estonian Research Council grant PRG1023 and project TT13. This project has received funding from the European Union's H2020 research and innovation program under Grant Agreement n° 952982.

Appendix A. Supplementary data

Supplementary data to this article can be found online at https://doi.org/10.1016/j.solmat.2023.112182.

References

[1] S. Hadke, M. Huang, C. Chen, Y.F. Tay, S. Chen, J. Tang, L. Wong, Emerging Chalcogenide Thin Films for Solar Energy Harvesting Devices, (n.d.). https://doi.org/10.1021/acs.chemrev.1c00301.

[2] A. Mule, B. Vermang, M. Sylvester, G. Brammertz, S. Ranjbar, T. Schnabel, N. Gampa, M. Meuris, J. Poortmans, Effect of different alkali (Li, Na, K, Rb, Cs) metals on $Cu_2ZnSnSe_4$ solar cells, Thin Solid Films 633 (2017) 156–161, https://doi.org/10.1016/j.tsf.2016.11.027.

[3] Y.E. Romanyuk, S.G. Haass, S. Giraldo, M. Placidi, D. Tiwari, D.J. Fermin, X. Hao, H. Xin, T. Schnabel, M. Kauk-Kuusik, P. Pistor, S. Lie, L.H. Wong, Doping and alloying of kesterites, J.Phys.Energy 1 (2019), https://doi.org/10.1088/2515-7655/ab23bc.

[4] P. Jackson, R. Wuerz, D. Hariskos, E. Lotter, W. Witte, M. Powalla, Effects of heavy alkali elements in $Cu(In,Ga)Se_2$ solar cells with efficiencies up to 22.6, Phys. Status Solidi Rapid Res. Lett. 10 (2016) 583–586, https://doi.org/10.1002/pssr.201600199.

[5] T. Schwarz, O. Cojocaru-Mirédin, P. Choi, M. Mousel, A. Redinger, S. Siebentritt, D. Raabe, Atom probe tomography study of internal interfaces in $Cu_2ZnSnSe_4$ thin-films, J. Appl. Phys. 118 (2015), https://doi.org/10.1063/1.4929874.

[6] M. Tsuyoshi, K. Atsuhito, W. Takahiro, First-principles study on alkali-metal effect of Li, Na, and K in $CuInSe_2$ and $CuGaSe_2$, Jpn. J. Appl. Phys. 54 (2015), 08KC20. http://stacks.iop.org/1347-4065/54/i=8S1/a=08KC20.

[7] D.R. Lide, S.R. Data, E.A. Board, G. Baysinger, S. Chemistry, C.E. Library, L. I. Berger, R.N. Goldberg, B. Division, H.V. Kehiaian, K. Kuchitsu, G. Rosenblatt, D. L. Roth, D. Zwillinger, CRC Handbook of Chemistry and Physics, 2004, p. 2660.

[8] X.F. Dong, T.T. Zheng, F.X. Yang, X.D. Sun, L. Yu, J.T. Chen, C.W. Wang, Y. Zhao, Y. Li, An effective Li-containing interfacial-treating strategy for performance enhancement of air-processed CZTSSe solar cells, Sol. Energy Mater. Sol. Cells 227 (2021), 111102, https://doi.org/10.1016/j.solmat.2021.111102.

[9] M. He, X. Zhang, J. Huang, J. Li, C. Yan, J. Kim, Y.S. Chen, L. Yang, J.M. Cairney, Y. Zhang, S. Chen, J. Kim, M.A. Green, X. Hao, High efficiency $Cu_2ZnSn(S,Se)_4$ solar cells with shallow LiZn acceptor defects enabled by solution-based Li post-deposition treatment, Adv. Energy Mater. 11 (2021) 2–9, https://doi.org/10.1002/aenm.202003783.

[10] Y. Yang, X. Kang, L. Huang, D. Pan, Tuning the band gap of $Cu_2ZnSn(S,Se)_4$ thin films via lithium alloying, ACS Appl. Mater. Interfaces 8 (2016) 5308–5313, https://doi.org/10.1021/acsami.5b11535.

[11] A. Lafond, C. Guillot-Deudon, J. Vidal, M. Paris, C. La, S. Jobic, Substitution of Li for Cu in Cu_2ZnSnS_4: toward wide band gap absorbers with low cation disorder for thin film solar cells, Inorg. Chem. 56 (2017) 2712–2721, https://doi.org/10.1021/acs.inorgchem.6b02865.

[12] J. Zhou, X. Xu, B. Duan, H. Wu, J. Shi, Y. Luo, D. Li, Q. Meng, Regulating crystal growth via organic lithium salt additive for efficient Kesterite solar cells, Nano Energy 89 (2021), 106405, https://doi.org/10.1016/j.nanoen.2021.106405.

[13] X. Li, M. Pilvet, K. Timmo, M. Grossberg, M. Danilson, V. Mikli, M. Kauk-Kuusik, Effect of absorber surface modification on the optoelectronic properties of $Cu_2CdGeSe_4$ solar cells, Thin Solid Films 697 (2020), https://doi.org/10.1016/j.tsf.2020.137822.

[14] H. Xin, S.M. Vorpahl, A.D. Collord, I.L. Braly, A.R. Uhl, B.W. Krueger, D.S. Ginger, H.W. Hillhouse, Lithium-doping inverts the nanoscale electric field at the grain boundaries in $Cu_2ZnSn(S,Se)_4$ and increases photovoltaic efficiency, Phys. Chem. Chem. Phys. 17 (2015) 23859–23866, https://doi.org/10.1039/c5cp04707b.

[15] Y. Yang, L. Huang, D. Pan, New insight of Li-doped $Cu_2ZnSn(S,Se)_4$ thin films: Li-induced Na diffusion from soda lime glass by a cation-exchange reaction, ACS Appl. Mater. Interfaces 9 (2017) 23878–23883, https://doi.org/10.1021/acsami.7b07796.

[16] M. Kauk-Kuusik, K. Timmo, K. Muska, M. Pilvet, J. Krustok, M. Danilson, V. Mikli, R. Josepson, M. Grossberg-Kuusk, Reduced recombination through CZTS/CdS interface engineering in monograin layer solar cells, J.Phys.Energy 4 (2022) 1–14, https://doi.org/10.1088/2515-7655/ac618d.

[17] R. Sridhar, C.E. Johnson, E.J. Cairns, Phase diagrams of the systems lil-KI and lil-rbl, J. Chem. Eng. Data 15 (1970) 244–245, https://doi.org/10.1021/je60045a027.

[18] Q. Gong, W. Ding, A. Bonk, H. Li, K. Wang, A. Jianu, A. Weisenburger, A. Bund, T. Bauer, Molten iodide salt electrolyte for low-temperature low-cost sodium-based liquid metal battery, J. Power Sources 475 (2020), 228674, https://doi.org/10.1016/j.jpowsour.2020.228674.

[19] E. Mellikov, M. Altosaar, M. Kauk-Kuusik, K. Timmo, D. Meissner, M. Grossberg, J. Krustok, O. Volobujeva, Growth of CZTS-based monograins and their application to membrane solar cells, copp. Zinc tin sulfide-based thin-film, Sol. Cell. (2015) 289–309, https://doi.org/10.1002/9781118437865.ch13.

[20] M. Kauk-Kuusik, X. Li, M. Pilvet, K. Timmo, M. Grossberg, T. Raadik, M. Danilson, V. Mikli, M. Altosaar, J. Krustok, J. Raudoja, Study of $Cu_2CdGeSe_4$ monograin powders synthesized by molten salt method for photovoltaic applications, Thin Solid Films 666 (2018) 15–19, https://doi.org/10.1016/j.tsf.2018.09.025.

[21] M. Kauk-Kuusik, K. Timmo, K. Muska, M. Pilvet, J. Krustok, R. Josepson, G. Brammertz, B. Vermang, M. Danilson, M. Grossberg, Detailed insight into the CZTS/CdS interface modification by air annealing in monograin layer solar cells, ACS Appl. Energy Mater. 4 (2021) 12374–12382, https://doi.org/10.1021/acsaem.1c02186.

[22] J. He, L. Sun, S. Chen, Y. Chen, P. Yang, J. Chu, Composition dependence of structure and optical properties of $Cu_2ZnSn(S,Se)_4$ solid solutions: an experimental study, J. Alloys Compd. 511 (2012) 129–132, https://doi.org/10.1016/j.jallcom.2011.08.099.

[23] H. Guo, G. Wang, R. Meng, Y. Sun, S. Wang, S. Zhang, J. Wu, L. Wu, G. Liang, H. Li, Y. Zhang, An efficient Li+-doping strategy to optimize the band alignment of a $Cu_2ZnSn(S,Se)_4$/CdS interface by a Se&LiF co-selenization process, J. Mater. Chem. 8 (2020) 22065–22074, https://doi.org/10.1039/d0ta07268k.

[24] A. Cabas-Vidani, S.G. Haass, C. Andres, R. Caballero, R. Figi, C. Schreiner, J. A. Márquez, C. Hages, T. Unold, D. Bleiner, A.N. Tiwari, Y.E. Romanyuk, High-efficiency $(Li_xCu_{1-x})_2ZnSn(S,Se)_4$ kesterite solar cells with lithium alloying, Adv. Energy Mater. 8 (2018) 1–8, https://doi.org/10.1002/aenm.201801191.

[25] M. Dimitrievska, A. Fairbrother, X. Fontané, T. Jawhari, V. Izquierdo-Roca, E. Saucedo, A. Pérez-Rodríguez, Multiwavelength excitation Raman scattering study of polycrystalline kesterite Cu_2ZnSnS_4 thin films, Appl. Phys. Lett. 104 (2014), https://doi.org/10.1063/1.4861593.

[26] M. Grossberg, J. Krustok, T. Raadik, M. Kauk-Kuusik, J. Raudoja, Photoluminescence study of disordering in the cation sublattice of Cu_2ZnSnS_4, Curr. Appl. Phys. 14 (2014) 1424–1427, https://doi.org/10.1016/j.cap.2014.08.013.

[27] K. Timmo, M. Altosaar, M. Kauk, J. Raudoja, E. Mellikov, $CuInSe_2$ monograin growth in the liquid phase of potassium iodide, Thin Solid Films 515 (2007) 5884–5886, https://doi.org/10.1016/j.tsf.2006.12.085.

[28] T. Schmidt, K. Lischka, W. Zulehner, Excitation-power dependence of the near-band-edge photoluminescence of semiconductors, Phys. Rev. B 45 (1992) 8989–8994, https://doi.org/10.1103/PhysRevB.45.8989.

[29] J. Krustok, H. Collan, M. Yakushev, K. Hjelt, The role of spatial potential fluctuations in the shape of the PL bands of multinary semiconductor compounds, Phys. Scr., T 79 (1999) 179–182, https://doi.org/10.1238/physica.topical.079a00179.

[30] J. Krustok, H. Collan, K. Hjelt, Does the low-temperature Arrhenius plot of the photoluminescence intensity in CdTe point towards an erroneous activation energy? J. Appl. Phys. 81 (1997) 1442–1445, https://doi.org/10.1063/1.363903.

[31] J. Krustok, J. Raudoja, M. Krunks, H. Mändar, H. Collan, Nature of the native deep localized defect recombination centers in the chalcopyrite and orthorhombic $AgInS_2$, J. Appl. Phys. 88 (2000) 205–209, https://doi.org/10.1063/1.373644.

[32] J. Krustok, J. Raudoja, J.H. Schön, M. Yakushev, H. Collan, Role of deep donor-deep acceptor complexes in CIS-related compounds, Thin Solid Films 361 (2000) 406–410, https://doi.org/10.1016/S0040-6090(99)00756-7.

[33] E. Kask, J. Krustok, S. Giraldo, M. Neuschitzer, S. López-Marino, E. Saucedo, Temperature dependent electrical characterization of thin film $Cu_2ZnSnSe_4$ solar cells, J. Phys. D Appl. Phys. 49 (2016), 85101, https://doi.org/10.1088/0022-3727/49/8/085101.

[34] J. Krustok, R. Josepson, T. Raadik, M. Danilson, Potential fluctuations in $Cu_2ZnSnSe_4$ solar cells studied by temperature dependence of quantum efficiency curves, Phys. B Condens. Matter 405 (2010) 3186–3189, https://doi.org/10.1016/j.physb.2010.04.041.

[35] M. Buffière, G. Brammertz, A.-A. El Mel, N. Lenaers, Y. Ren, A.E. Zaghi, Y. Mols, C. Koeble, J. Vleugels, M. Meuris, J. Poortmans, Minority Carrier Lifetime Stability in Polycrystalline $Cu_2ZnSnSe_4$ Thin Films, ((n.d.)).

[36] M. Grossberg, J. Krustok, C.J. Hages, D.M. Bishop, O. Gunawan, R. Scheer, S. M. Lyam, H. Hempel, S. Levcenco, T. Unold, The electrical and optical properties of kesterites, J.Phys.Energy 1 (2019), https://doi.org/10.1088/2515-7655/ab29a0.